

NO-A176 378

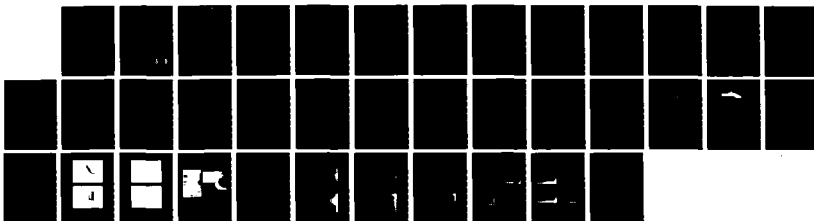
SOLUTION OF THE THREE-DIMENSIONAL NAVIER-STOKES
EQUATIONS FOR A TURBULENT.. (U) SCIENTIFIC RESEARCH
ASSOCIATES INC GLASTONBURY CT R C BUGGELIN ET AL

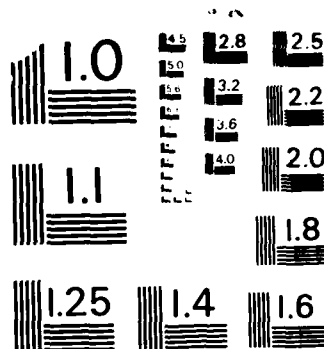
1/1

UNCLASSIFIED

JAN 87 SRA-R87-920027-F N00014-85-C-0420 F/G 20/4

NL





MICROCOPY RESOLUTION TEST CHART
NATIONAL BUREAU OF STANDARDS-1963-A

12

Report R87-920027-F

SOLUTION OF THE THREE-DIMENSIONAL NAVIER-STOKES
EQUATIONS FOR A TURBULENT HORSESHOE VORTEX FLOW

R. C. Ruggeln, W. R. Briley and H. McDonald
Scientific Research Associates, Inc.
P.O. Box 1058
Glastonbury, CT 06033

January 1987

Final Report for Period 1 October 1985 - 30 September 1986

Approved for Public Release; Distribution Unlimited

UIC FILE COPY

Prepared for:

OFFICE OF NAVAL RESEARCH
800 No. Quincy Street
Arlington, VA 22217

DTIC
ELECTE
FEB 04 1987
S D
E

AD-A176 370

Unclassified

SECURITY CLASSIFICATION OF THIS PAGE

AD-A176370

REPORT DOCUMENTATION PAGE

1a. REPORT SECURITY CLASSIFICATION Unclassified			1b. RESTRICTIVE MARKINGS			
2a. SECURITY CLASSIFICATION AUTHORITY			3. DISTRIBUTION/AVAILABILITY OF REPORT Approved for Public Release; Distribution Unlimited			
2b. DECLASSIFICATION/DOWNGRADING SCHEDULE						
4. PERFORMING ORGANIZATION REPORT NUMBER(S) R87-920027-F			5. MONITORING ORGANIZATION REPORT NUMBER(S)			
6a. NAME OF PERFORMING ORGANIZATION Scientific Research Associates, Inc.		6b. OFFICE SYMBOL (If applicable)	7a. NAME OF MONITORING ORGANIZATION Office of Naval Research			
6c. ADDRESS (City, State and ZIP Code) 50 Nye Rd. (P.O. Box 1058) Glastonbury, CT 06033			7b. ADDRESS (City, State and ZIP Code) 800 N. Quincy Street Arlington, VA 22217			
8a. NAME OF FUNDING/SPONSORING ORGANIZATION		8b. OFFICE SYMBOL (If applicable)	9. PROCUREMENT INSTRUMENT IDENTIFICATION NUMBER N00014-85-C-0420			
8c. ADDRESS (City, State and ZIP Code) Solution of the Three-Dimensional Navier-Stokes Equations for a Turbulent Horseshoe Vortex Flow			10. SOURCE OF FUNDING NOS.			
			PROGRAM ELEMENT NO.	PROJECT NO.	TASK NO.	WORK UNIT NO.
11. TITLE (Include Security Classification) Vortex Flow						
12. PERSONAL AUTHOR(S) Buggeln, R.C., Briley, W.R., McDonald, H.						
13a. TYPE OF REPORT Final		13b. TIME COVERED FROM 85/10 TO 86/9		14. DATE OF REPORT (Yr., Mo., Day) 1987, January		15. PAGE COUNT 34
16. SUPPLEMENTARY NOTATION						
17. COSATI CODES			18. SUBJECT TERMS (Continue on reverse if necessary and identify by block number)			
FIELD	GROUP	SUB. GR.	Three-Dimensional Flow Horseshoe Vortex Flow			
			Navier-Stokes Equations Implicit Algorithm			
			Turbulent Flow			
19. ABSTRACT (Continue on reverse if necessary and identify by block number) The problem of three-dimensional turbulent horseshoe-vortex/corner flow is investigated numerically. Solutions of the compressible Reynolds-averaged Navier-Stokes equations are computed using a linearized block implicit scheme with Douglas Gunn splitting. Solutions are computed using both two-equation (k-ε) and algebraic mixing length turbulence models, with grid distributions which provide resolution of the viscous sublayer regions. These computed results are displayed graphically and compared with recent experimental measurements of McMahon, Hubbartt and Kubendran. There is good qualitative agreement between computed and measured mean flow velocities, especially near the saddle point separation line. The computed corner flow has a multiple vortex structure. There are quantitative differences in details of the weak corner flows downstream of the leading edge, which may be attributable to the turbulence model used and/or numerical error. Convergence required approximately 150 iterations using a 60x50x40 grid (120,000 points) and required about 2.5 hours of CRAY-XMP run time.						
20. DISTRIBUTION/AVAILABILITY OF ABSTRACT UNCLASSIFIED/UNLIMITED <input type="checkbox"/> SAME AS RPT. <input checked="" type="checkbox"/> DTIC USERS <input type="checkbox"/>			21. ABSTRACT SECURITY CLASSIFICATION Unclassified			
22a. NAME OF RESPONSIBLE INDIVIDUAL			22b. TELEPHONE NUMBER (Include Area Code)		22c. OFFICE SYMBOL	

ABSTRACT

The problem of three-dimensional turbulent horseshoe-vortex/corner flow is investigated numerically. Solutions of the compressible Reynolds-averaged Navier-Stokes equations are computed using a linearized block implicit scheme with Douglas Gunn splitting. Solutions are computed using both two-equation (k-ε) and algebraic mixing length turbulence models, with grid distributions which provide resolution of the viscous sublayer regions. These computed results are displayed graphically and compared with recent experimental measurements of McMahon, Hubbarth and Kubendran. There is good qualitative agreement between computed and measured mean flow velocities, especially near the saddle point separation line. The computed corner flow has a multiple vortex structure. There are quantitative differences in details of the weak corner flows downstream of the leading edge, which may be attributable to the turbulence model used and/or numerical error. Convergence required approximately 150 iterations using a 60×50×40 grid (120,000 points) and required about 2.5 hours of CRAY-XMP run time.

Accession For	
NTIS GRA&I	<input checked="" type="checkbox"/>
DTIC TAB	<input checked="" type="checkbox"/>
Unannounced	<input type="checkbox"/>
Justification	
By _____	
Distribution/	
Availability Codes	
Dist	Avail and/or Special
A-1	



INTRODUCTION.

The horseshoe-vortex and associated corner flows which occur when a blunt obstruction is placed within an approaching boundary layer represent a fundamental three-dimensional viscous flow of considerable interest and importance. Examples of this type of flow include the flows near an aircraft wing/fuselage junction and near a submarine hull/sail junction. The feature common to all horseshoe vortex flows is that a non-uniform velocity in an approaching boundary layer meets a local region of adverse pressure gradient due to the blockage effect of the obstruction. This causes a three-dimensional boundary layer separation and the formation of one or more horseshoe vortices around the obstruction. In addition to the leading edge region, the associated corner flows downstream of the leading edge are also of interest, since they contain streamwise vortices which affect the performance of both the airfoil or strut and also other devices located downstream.

The problem of horseshoe-vortex/corner flow has been investigated previously [1-2] by numerical solution of the Navier-Stokes equations using a linearized block implicit (LBI) scheme with Douglas-Gunn splitting. Solutions for laminar flow past an elliptical leading edge mounted normal to a flat plate endwall have been computed for both zero and five-degree angles of incidence, with chordal Reynolds number of 400, and Mach number of 0.2. Turbulent flow cases have been computed for both unswept and 45-degree swept elliptical leading edges mounted on a flat plate, with Reynolds number of 310,000 and Mach number of 0.05. More recently, Briley, Buggeln and McDonald [3] have found that appropriate inflow/outflow boundary conditions provide conditional stability and rapid convergence for the three-dimensional algorithm and have considered alternative forms of artificial dissipation. An accurate (grid insensitive) solution was computed for a laminar horseshoe vortex flow using only small amounts of artificial dissipation. Very good convergence rates were obtained for this laminar flow case, with residuals reduced by a factor of 10^{-2} in 30 and 60 iterations, respectively, for $15 \times 15 \times 15$ and $30 \times 30 \times 30$ grids. This work is extended in the present study to address turbulent flows using both two-equation ($k-\epsilon$) and algebraic mixing length turbulence models, with viscous sublayer resolution.

Recent experimental work on turbulent horseshoe vortex flows includes that of McMahon, Hubhart and Kubendran [4], Moore and Forlini [5], Eckerle and

Langston [6] and Dickinson [7]. Moore and Moore [8] have performed numerical computations using the inviscid Euler equations for a horseshoe vortex flow and have compared these results with the measurements of Moore and Forlini [5]. Calculations for a blunt-fin induced shock wave and boundary layer interaction flow containing a horseshoe vortex have been reported by Hung and Kordulla [9].

In the present report, the methods used in solving the three-dimensional Navier-Stokes equations and two-equation turbulence model are first reviewed. Turbulence models based on solution of the k - ϵ equations and on an algebraic mixing length model are then implemented within a vectorized code using coordinate distributions which provide resolution of viscous sublayer regions. Resolution of the viscous sublayer region is believed to be important for three-dimensional flows, for which wall-function boundary conditions are of limited value. Test calculations are then performed for a two-dimensional turbulent flow to develop the computational methodology necessary to obtain rapid convergence. Finally, three-dimensional turbulent horseshoe vortex flows are computed using both k - ϵ and mixing length models. These results are displayed graphically and are evaluated by comparison with recent detailed experimental measurements obtained by McMahon, Hubbarth and Kubendran [4].

GOVERNING EQUATIONS

The three-dimensional compressible Navier-Stokes equations are solved here for low Mach number and with an assumption of constant stagnation enthalpy. For these conditions, steady flow solutions closely approximate an incompressible constant density flow (cf. Briley, McDonald and Shamroth [10]). A zonal approach is used wherein the flow is computed only in a subregion of the overall flow field, near the leading edge (Fig. 1). The form of the governing equations solved permits the use of general nonorthogonal body-fitted coordinate systems, and is obtained by a transformation from Cartesian to general nonorthogonal coordinates. The Cartesian velocity components u_i and density ρ are retained as dependent variables in the transformed system of equations. The pressure, temperature and stagnation enthalpy are denoted p , T and h_0 , respectively.

All variables are nondimensional in the present formulation, having been normalized by reference quantities denoted by a subscript 'r'. The quantities ρ_r , U_r , T_r and L_r denote reference values for density, velocity, temperature

and length, respectively. The reference pressure, enthalpy and time are taken as $\rho_r U_r$, $c_p T_r$ and L_r/U_r , respectively, where c_p is the specific heat at constant pressure. The specific heat ratio is γ , and $M_r = U_r/c_r$ is a reference Mach number, where c_r is the reference sound speed defined by $c_r^2 = \gamma R T_r$, and R is the gas constant. The reference Reynolds number Re is defined by $\rho_r U_r L_r / \mu_r$, where μ_r is a reference viscosity.

The transformation, T , from Cartesian coordinates x_i to computational coordinates y^j is given by

$$T = y^j(x_i) \quad i, j = 1, 2, 3 \quad (1)$$

Spatial derivatives are transformed according to

$$\frac{\partial}{\partial x_i} = y^j_{,i} \frac{\partial}{\partial y^j} \quad (2)$$

where, unless otherwise stated, the summation convention is used for repeated indices, and $y^j_{,i} \equiv \partial y^j / \partial x_i$. The coordinate system is defined by specifying the Cartesian coordinates of each computational grid point. The partial derivatives $\partial x_i / \partial y^j$ of the inverse transformation $T^{-1} = x_i(y^j)$ are then computed using three-point second-order difference formulas with uniform spacing of the computational coordinates y^j . For convenience, the y^j coordinates are normalized to give a unit mesh spacing $\Delta y^j = 1$ for each coordinate. The transformation derivatives $\partial y^j / \partial x_i$ are then computed from $\partial x_i / \partial y^j$ using standard procedures for computing derivatives of inverse functions (cf. Kaplan [11]).

The transformed Navier-Stokes equations can be written in the following nondimensional form: The continuity equation is

$$\frac{\partial \rho}{\partial t} + y^j_{,i} \frac{\partial}{\partial y^j} \rho u_i = 0 \quad (3)$$

The k th component of the momentum equation is given by

$$\frac{\partial(\rho u_k)}{\partial t} + y^j_{,i} \frac{\partial}{\partial y^j} (\rho u_i u_k + \delta_{ik} p - \tau_{ik}) = 0 \quad (4)$$

where δ_{ik} is the Kronecker delta function. The shear stress τ_{ik} is given by

$$\tau_{ik} = \text{Re}^{-1} \left(y_{,k}^m \frac{\partial u_i}{\partial y^m} + y_{,i}^m \frac{\partial u_k}{\partial y^m} - \frac{2}{3} \delta_{ik} y_{,l}^m \frac{\partial u_l}{\partial y^m} \right) \quad (5)$$

The equation of state and definition of stagnation enthalpy can be expressed for a perfect gas as

$$p = \rho T / \gamma M_r^2 \quad (6)$$

$$h_o = T / (\gamma - 1) M_r^2 + q^2 / 2 \quad (7)$$

where $q^2 = \delta^{ij} u_i u_j$. Although it is not necessary, it is both convenient and computationally worthwhile for the present problem to assume that h_o is a constant and to omit solution of the energy equation. This results in negligible error for steady flow at low Mach number with no heat addition. Equations (6) and (7) can then be combined to produce an adiabatic equation of state

$$p = \rho (h_o - q^2 / 2) (\gamma - 1) / \gamma \quad (8)$$

which is used to eliminate pressure as a dependent variable in Eq. (4).

Two turbulence models have been utilized in the present investigation. These are a two-equation (k - ϵ) model based on that due to Jones and Launder [12], and a simple algebraic mixing length model. Each of these models is formulated to provide resolution of the viscous sublayer region near solid walls. The turbulent viscosity is assumed to be isotropic and is added to the laminar viscosity to obtain a total effective viscosity, $\mu_e = \mu + \mu_T$.

The governing turbulence kinetic energy (k) and dissipation rate (ϵ) are given by Launder and Spalding [13]. Applying the general coordinate transformation, these equations can be written as

$$\frac{\partial \rho k}{\partial t} + y_{,i}^j \frac{\partial}{\partial y^j} \left[\rho u_i k - \text{Re}^{-1} \left(\mu + \frac{\mu_T}{\sigma_k} \right) y_{,i}^m \frac{\partial k}{\partial y^m} \right] = P - \rho \epsilon \quad (9)$$

$$\frac{\partial \rho \epsilon}{\partial t} + y_{,i}^j \frac{\partial}{\partial y^j} \left[\rho u_i \epsilon - \text{Re}^{-1} \left(\mu + \frac{\mu_T}{\sigma_\epsilon} \right) y_{,i}^m \frac{\partial \epsilon}{\partial y^m} \right] = C_{1k} \frac{\epsilon}{k} P - C_{2k} \frac{\rho \epsilon^2}{k} \quad (10)$$

where P is the turbulence production given by

$$P = \text{Re}^{-1} \mu_T \left[2 D_{ij} D_{ij} - \frac{2}{3} \left(y_{,i}^j \frac{\partial u_i}{\partial y^j} \right)^2 \right] \quad (11)$$

and

$$D_{ij} = \frac{1}{2} \left(y_{,j}^m \frac{\partial u_i}{\partial y^m} + y_{,i}^m \frac{\partial u_j}{\partial y^m} \right) \quad (12)$$

These equations are supplemented by the Prandtl-Kolmogorov relation for turbulent viscosity

$$\text{Re}^{-1} \mu_T = C_\mu \rho k^2 / \epsilon \quad (13)$$

The following values for empirical constants were used (cf. Refs. 12, 13):

$$C_1 = 1.44 \quad (14a)$$

$$C_2 = 1.92 [1 - 0.3 \exp(-R_T^2)] \quad (14b)$$

$$C_\mu = 0.09 \exp[-2.5/(1 + R_T/50)] \quad (14c)$$

$$\sigma_k = 1.0 \quad (14d)$$

$$\sigma_\epsilon = 1.3 \quad (14e)$$

Where R_T is a turbulence Reynolds number defined as

$$R_T = \rho k^2 / \mu \epsilon \quad (15)$$

Jones and Launder [12] have suggested adding additional terms to the turbulence energy and dissipation equations for use in computing low Reynolds number turbulent flows. An extra term was added to the k equation for computational reasons to counteract the effect of applying $\epsilon = 0$ as a wall boundary condition. In the present study, these extra terms were omitted and a zero-gradient condition for ϵ was applied as a wall condition.

An algebraic mixing length model was used both for flow predictions and as a method of initializing the flow field and starting the k - ϵ model. In the mixing length model, the turbulent viscosity is obtained from

$$\mu_T = \rho \ell^2 (2D_{ij}D_{ij})^{1/2} \quad (16)$$

It remains to specify a length scale distribution appropriate for the problem under consideration. The horseshoe-vortex/corner flow of interest here has moderately thin shear layers on the endwall and strut surface, and the length scale distribution is thus adapted from previous turbulence models for turbulent boundary layers and taken to be the conventionally defined mixing length of Prandtl. The distribution of mixing length given by McDonald and Fish [14] has proven effective for a wide range of two-dimensional turbulent boundary layers and is easily adapted for present use. This distribution is given by

$$\ell = \mathcal{D} \ell_\infty \tanh (\kappa d / \ell_\infty) \quad (17)$$

where ℓ is mixing length, ℓ_∞ is an outer-region value of mixing length, d is distance from the wall, κ is the von Karman constant (taken here as 0.4), and \mathcal{D} is the Van Driest sublayer damping function given by

$$\mathcal{D} = 1 - \exp (-y^+ / A^+) \quad (18)$$

where

$$y^+ = du_w^* \rho / \mu \quad (19)$$

and $u_w^* = (\tau_w/\rho)^{1/2}$ and τ_w is the wall shear stress. The constant A^+ is taken as 26.0. For equilibrium boundary layers, the freestream mixing length, l_∞ is observed to have a constant value of about 0.1δ , where δ is the local boundary layer thickness.

The length scale distribution of Eq. (17) is adapted for present use by taking d as distance to the nearest wall and by assigning l_∞ a distribution based on two-dimensional momentum integral estimates of the boundary layer growth rates on the endwall. A constant value of freestream mixing length was used for the strut surface. Two boundary layer thickness distributions, δ_1 for the endwall boundary layer and δ_2 for the strut surface, are obtained and an outer or maximum mixing length scale associated with each boundary layer is determined from the formula $l_\infty = 0.1 \delta$. In the core region outside the boundary layer the length scale is exponentially damped to a negligible value over a distance of about two boundary layer thicknesses. In the overlap corner region, the outer or maximum length scale, l_∞ , is taken as the greater of the two values associated with the strut and endwall boundary layers.

METHOD OF SOLUTION

The basic algorithm considered here has been described by Briley and McDonald [15, 16] and employs a formal time linearization to produce a noniterative fully-coupled approximation for nonlinear systems of equations, which is solved in block-implicit form using an ADI scheme with consistent intermediate steps. For a linear scalar diffusion equation, this algorithm reduces to a classical ADI scheme considered by Douglas and Gunn [17]. Warming and Beam [18, 19] have introduced a very concise derivation of this same algorithm using approximate factorization of the linearized approximation written in 'delta' form. The works of Pulliam and Steger [20], Thomas and Lombard [21] and Shamroth, McDonald and Briley [22] are representative of numerous investigations which have employed this basic algorithm.

Linearization and Time Differencing

The nonlinear system of governing equations is first written (at a single grid point) in the following form:

$$\partial H(\phi)/\partial t = D(\phi) + S(\phi) \quad (20)$$

where ϕ is the column-vector of dependent variables, H and S are column-vector algebraic functions of ϕ , and D is a column vector whose elements are the spatial differential operators which generate all spatial derivatives appearing in the governing equation associated with that element.

The solution procedure is based on the following two-level implicit time-difference approximation of (20):

$$(H^{n+1} - H^n)/\Delta t = \beta(D^{n+1} + S^{n+1}) + (1-\beta)(D^n + S^n) \quad (21)$$

where, for example, H^{n+1} denotes $H(\phi^{n+1})$ and $\Delta t = t^{n+1} - t^n$. The parameter β ($0.5 < \beta < 1$) permits a variable time-centering of the scheme, with a truncation error of order $[\Delta t^2, (\beta - 1/2) \Delta t]$.

A local time linearization (Taylor expansion about ϕ^n) of requisite formal accuracy is introduced, and this serves to define a linear differential operator, L , such that

$$D^{n+1} = D^n + L^n (\phi^{n+1} - \phi^n) + O(\Delta t^2) \quad (22a)$$

Similarly,

$$H^{n+1} = H^n + (\partial H / \partial \phi)^n (\phi^{n+1} - \phi^n) + O(\Delta t^2) \quad (22b)$$

$$S^{n+1} = S^n + (\partial S / \partial \phi)^n (\phi^{n+1} - \phi^n) + O(\Delta t^2) \quad (22c)$$

Equations (22a-c) are inserted into Eq. (21) to obtain the following system which is linear in ϕ^{n+1}

$$(A - \beta \Delta t L^n) (\phi^{n+1} - \phi^n) = \Delta t (D^n + S^n) \quad (23)$$

and which is termed a linearized block implicit (LBI) scheme. Here, A denotes a square matrix defined by

$$A \equiv (\partial H / \partial \phi)^n - \beta \Delta t (\partial S / \partial \phi)^n \quad (24)$$

Equation (22) has $O(\Delta t)$ accuracy unless $H \equiv \phi$, in which case the accuracy is the same as Eq. (21).

Special Treatment of Diffusive Terms

Spatial cross-derivatives are present in viscous terms and in added artificial dissipation terms of the present formulation, and these cross derivative terms are evaluated explicitly at t^n . To preserve notational simplicity, it is understood that all cross-derivative terms appearing in L^n are neglected but are retained in D^n . In addition, although diffusion coefficients in viscous and dissipation terms are generally functions of the dependent variables, these coefficients are not linearized and instead are evaluated implicitly at t^n during each time step. Notationally, this is

equivalent to neglecting derivatives of these coefficients with respect to ϕ in L^n , which are formally present in the Taylor expansion (22a), but otherwise retaining all terms in both L^n and D^n .

It is important to note that neglecting terms in L^n has no effect on steady solutions of Eq. (23), since $\phi^{n+1} - \phi^n \equiv 0$ and thus Eq. (23) reduces to the steady form of the equations: $D^n + S^n = 0$. Aside from stability considerations, the only effect of neglecting terms in L^n is to introduce an $O(\Delta t)$ truncation error.

Consistent Splitting of the LBI Scheme

To obtain an efficient algorithm, the linearized system (23) is split using ADI techniques. To obtain the split scheme, the multidimensional operator, L , is rewritten as the sum of three "one-dimensional" sub-operators L_i ($i = 1, 2, 3$) each of which contains all terms having derivatives with respect to the i -th spatial coordinate. The split form of Eq. (23) can be derived either by following the procedure described by Douglas and Gunn in their generalization and unification of scalar ADI schemes, or using approximate factorization. In either case, for the present system of equations the split algorithm is given by

$$(A - \beta \Delta t L_1^n) (\phi^* - \phi^n) = \Delta t (D^n + S^n) \quad (25a)$$

$$(A - \beta \Delta t L_2^n) (\phi^{**} - \phi^n) = A (\phi^* - \phi^n) \quad (25b)$$

$$(A - \beta \Delta t L_3^n) (\phi^{n+1} - \phi^n) = A (\phi^{**} - \phi^n) \quad (25c)$$

where ϕ^* and ϕ^{**} are consistent intermediate solutions. If spatial derivatives appearing in L_i and D are replaced by three-point difference formulas, then each step in Eqs. (25a-c) can be solved by a block-tridiagonal elimination.

Combining Eqs. (25a-c) gives

$$\begin{aligned} & (A - \beta \Delta t L_1^n) A^{-1} (A - \beta \Delta t L_2^n) A^{-1} (A - \beta \Delta t L_3^n) (\phi^{n+1} - \phi^n) \\ & = \Delta t (D^n + S^n) \end{aligned} \quad (26)$$

which approximates the unsplit scheme (22) to $O(\Delta t^2)$. Since the intermediate steps are also consistent approximations for Eq. (22), physical boundary conditions can be used for ϕ^* and ϕ^{**} . Finally, since the L_i are homogeneous operators, it follows from Eq. (25a-c) that steady solutions have the property that $\phi^{n+1} = \phi^* = \phi^{**} = \phi^n$ and satisfy

$$D^n + S^n = 0 \quad (27)$$

The steady solution thus depends only on the spatial difference approximation used for (27), and does not depend on the solution algorithm itself.

In applying the split LBI scheme to the turbulence kinetic energy equation, it should be noted that the linearization employed by the viscous terms (turbulent viscosity is evaluated explicitly at t^n) decouples the turbulence equations from the continuity and momentum equations. This means that the two turbulence-model equations can be solved as a separate 2×2 coupled system, once the continuity and momentum equations have been solved. The turbulence kinetic energy and dissipation equations contain highly nonlinear source terms (RHS of Eqs. 9-10) which require linearization for implementation of the LBI scheme. These source terms are first rewritten utilizing Eqs. (11) and (13) to give

$$S(\phi) = \begin{bmatrix} 2Re^{-1}\mu_T D_{ij} D_{ij} - \rho \epsilon \\ C_\mu C_1 D_{ij} D_{ij} \rho k - C_2 \rho \epsilon^2 / k \end{bmatrix} \quad (28)$$

The last term in Equation (11) is negligible for low Mach number flows and has been neglected. These source terms are then linearized as follows:

$$\frac{\partial S}{\partial \phi} = \begin{bmatrix} 0 & -\rho \\ C_\mu C_1 D_{ij} D_{ij} \rho + C_2 \left(\frac{\epsilon^2}{k}\right), & -2C_2 \rho \left(\frac{\epsilon}{k}\right) \end{bmatrix} \quad (29)$$

COMPUTED RESULTS FOR A TURBULENT HORSESHOE VORTEX FLOW

Flow Conditions

Solutions are presented here for turbulent flow at zero incidence past an elliptical leading edge geometry mounted between parallel flat plate endwalls. The leading-edge geometry for the present calculations is the same as that considered by McMahon, Hubharrt and Kubendran [4] for turbulent flow conditions. The flow geometry (Fig. 1) consists of a strut of constant thickness, W , having an elliptical leading edge with 1.5:1 ratio of major to minor axis. The strut is mounted normal to parallel flat plate endwalls whose separation distance is $5.0W$, and whose leading edges are located a distance $6.0W$ upstream of the leading edge of the strut. The length L of the strut within the computational domain is $2.5W$. The flow considered has a Reynolds number $Re = 57,000$ (based on L) and Mach number $M_\infty = 0.05$, each based on upstream flow conditions.

Boundary Conditions

Since the computational domain is chosen to be a region in the immediate vicinity of the leading-edge/corner flow geometry (cf. Fig. 1) embedded within a larger overall flow system, inflow and outflow boundary conditions which adequately model the interface between the computed flow and the remainder of the flow system are required. The inflow/outflow conditions used are derived from an assumed flow structure and are chosen to provide inflow with prescribed stagnation pressure (and stagnation enthalpy) in an inviscid core region and with a given axial velocity profile shape in the endwall boundary layer, and to provide outflow with a prescribed distribution of static pressure in the cross section. This approach to inflow/outflow boundary conditions has been discussed previously in [1-2] and is only summarized here.

First, the boundary layer thickness $\delta(x_1)$ on the endwall flat plate is approximated by its distribution from the Blasius flat plate solution. At the inflow boundary, a "two-layer" boundary condition is employed such that stagnation pressure, p_0 , is fixed at the free stream reference value in the core flow region ($y^3 > \delta$) and an axial velocity profile shape $u_1/u_\infty = f(y^3/\delta)$

is fixed within the boundary layer region ($y^3 < \delta$). Here, u_e is the local edge velocity which varies with time and is adjusted after each time step to the value consistent with p_0 and the local edge static pressure, which is determined as part of the solution. The remaining inflow conditions are $u_2 = \partial^2 u_3 / \partial n^2 = \partial^2 p / \partial n^2 = 0$, where n denotes the normal computational coordinate, y^1 . For outflow conditions, a constant static pressure is imposed, and second derivatives of each velocity component are set to zero. At no-slip surfaces, each velocity component u_i is set to zero, and the remaining condition applied to these surfaces is that the derivative of pressure in the direction normal to the surface is zero. This condition approximates the normal momentum equation to order Re^{-1} for viscous flow at a no-slip surface. The final boundary to be considered is the plane parallel to the endwall and in the free stream. This boundary is assumed to be a plane of symmetry, so that the flow represented is that past the strut mounted between parallel flat plates.

Although a uniform grid was used for the transformed coordinates y^j , the grid used is highly nonuniform in physical coordinates x_i , as shown in Fig. 1, and was chosen to provide resolution of several length scales known to be present for this type of flow. Care was taken to provide resolution of the boundary layers and viscous sublayers on the strut and endwall surfaces of the shear layer near the leading-edge stagnation line, and of the corner flow region very near the endwall/leading-edge intersection.

A pseudo-time dependent iteration procedure was employed in which the square matrix A in the LBI scheme (25) is replaced by a modified matrix $A + AB$, where B is a diagonal conditioning matrix. This technique was employed by Briley, McDonald and Shamroth [10] to improve the convergence rate of this algorithm when applied to low Mach number flows. In the present calculations, a diagonal matrix B whose diagonal elements are $(1/\gamma M_\infty^2, 1, 1, 1)$ was used. In addition, a spatially varying time step was used to avoid instability analogous to that encountered for the three-dimensional scalar convection equation, and to improve the convergence rate.

Computed Results

Test calculations were performed for a two-dimensional turbulent flow to develop the computational methodology necessary to obtain rapid convergence using the two-equation turbulence model and coordinate distributions which

provide resolution of viscous sublayer regions. The test problem has the same geometry and flow conditions as the horseshoe vortex flow to be considered subsequently, but is restricted to the two-dimensional region away from the strut endwall intersection where the horseshoe vortex forms. The flow conditions for these test calculations are Reynolds number $Re = 57,000$ based on body width and inflow Mach number $M_\infty = 0.05$. A 60×50 grid was used, with a coordinate stretching such that the mesh spacing adjacent to the wall is approximately 0.0005. The coordinates and steady flow solution for these calculations are shown in Fig. 2.

The Mach number contours in Fig. 2 give an indication of the thin boundary layer associated with turbulent flow at this Reynolds number. Plots of maximum normalized residual and maximum increment of solution variable versus iteration number are shown in Figs. 3-4 for both mixing length and $k-\epsilon$ turbulence models. A dissipation parameter ($\sigma = 0.1$) was used for each of these calculations. The use of larger values of dissipation did not have a substantial effect on the convergence behavior. It should be noted that for scalar convection in one dimension, the value $\sigma = 1.0$ is equivalent to two-point upwind differencing, and thus the value $\sigma = 0.1$ is relatively small. In the mixing length calculations, the residual was reduced by a factor of about 10^5 in 100 iterations. The $k-\epsilon$ model was started after 25 iterations using the mixing length model, and although the convergence was not as fast as using the mixing length, the residual was reduced by about three orders of magnitude in 100 iterations. It is not clear whether the difference in convergence behavior between these two cases is due to the physical/mathematical properties of the $k-\epsilon$ turbulence model or to details of the numerical solution procedure. These calculations required about 27 seconds of CRAY-XMP CPU time using a vectorized code.

Solutions for three-dimensional horseshoe vortex flow were computed using both mixing length and $k-\epsilon$ turbulence models. The geometry and flow conditions correspond to those measured by McMahon, Hubbarth and Kubendran (Ref. 4). The Reynolds number is $Re = 57,000$ and a near incompressible Mach number $M_\infty = 0.05$ was used. The endwall boundary layer has a thickness of about $0.45 W$ at a distance of $3 W$ upstream of the leading edge. A $60 \times 50 \times 40$ grid (120,000 points) was used, with mesh spacings of $0.00075 W$ and $0.0005 W$ adjacent to the endwall and strut surfaces, respectively. The overall computational domain extended to a distance of $3.5 W$ from the endwall and strut surfaces, where symmetry

conditions were applied. Allowing for symmetry, the overall domain ($7 W \times 7 W$) is smaller than the wind tunnel cross section ($18.5 W \times 18.8 W$) in Ref. 4, and hence there is a stronger blockage effect in the computed results due to the body in the region downstream of the leading edge. The $k-\epsilon$ model was started after 100 iterations using the mixing length model, and convergence to three orders of residual reduction required about 200 iterations in three dimensions. In the three-dimensional $k-\epsilon$ calculations it was found necessary to use a larger dissipation parameter ($\sigma = 1.0$) than in the mixing length calculations ($\sigma = 0.1$). These solutions required about 2.5 hours of CRAY-XMP CPU time on a vectorized code, using 120,000 grid points.

The computed flow behavior using the $k-\epsilon$ turbulence model is first discussed and compared with experimental measurements. A comparison of the $k-\epsilon$ and mixing length solutions will be given subsequently. Some computer-generated flow visualization results are given in Figs. 5a-b. The computational grid shown is the grid used for the solution, except that approximately one-half of the grid points in each direction have been omitted. The contours of surface pressure show the three-dimensional behavior, with low pressure near the leading-edge/endwall intersection. The particle path lines shown are useful as a visualization of the three-dimensional horseshoe vortex flow structure. Two groups of particle lines are shown. The first group includes particle lines which originate at the upstream inflow boundary in a line of points parallel to the endwall and located very near the endwall. These particle lines remain very close to the endwall but are deflected at the saddle-point separation line and remain outside the horseshoe vortex. The second group of particle lines originates from a vertical line of points located near the plane of symmetry and just upstream of the leading edge. These particle lines originate behind the saddle-point separation and show the downward flow near the intersection of the leading edge and endwall surfaces. Some of these particle lines near the endwall flow in a direction opposite the freestream and toward the saddle-point separation line and then remain near this separation line downstream of the leading edge. The remaining particle lines stay much closer to the body surface. The overall flow behavior revealed by these computer-generated particle lines is very similar to that observed in numerous flow visualization experiments for horseshoe vortex flows of this type.

The computed flow near the strut/endwall intersection is compared with surface oil-flow visualization photographs in Fig. 6. Vector velocity plots in the plane of grid points adjacent to the no-slip endwall surface are shown, together with the selected streamlines. A saddle-point flow separation and reverse flow region are clearly visible in both computed and experimental results and there is good agreement in the location of this separation point. The experimental flow visualization has a second saddle-point separation located near the leading edge. The computed flow also has a second saddle-point separation, although it is located much closer to the leading edge than that evident in the flow visualization and is not clearly visible in Fig. 6.

McMahon, Hubbarth and Kubendran (Ref. 4) measured streamwise and transverse velocity components at streamwise stations both upstream and downstream of the strut leading edge, as indicated in Fig. 7. The computed mean flow velocities at three of the measured stations are compared with these measurements in Figs. 8a-c. The comparison at station 3, located 11 mm upstream of the leading edge, is shown in Fig. 8a. This station is located within the reversed flow region of the saddle-point flow separation and a small reversed flow region can be seen in the computed streamwise velocity contours. In general, there is good agreement between computed and measured mean flow velocities. The computed and measured transverse velocity vectors generally agree as to strength, direction and skewing near the wall. The computed and measured velocities at stations 4 and 5, located in the corner region downstream of the leading edge, are shown in Figs. 8b and 8c. Although the strength of the secondary flow is approximately correct, the details of the corner vortex and the distortion of the streamwise velocity contours by the corner vortex are not accurately predicted. It should be noted that the computed flow has increased blockage effects since the computed flow region is smaller than the wind tunnel cross section, as mentioned earlier. It should also be noted that the corner vortex is relatively weak, with transverse velocities on the order of 5 percent of the streamwise velocity. It seems likely that the $k-\epsilon$ turbulence model used is inadequate for the corner flow region, although numerical truncation error may also affect this comparison despite the relatively high grid resolution in this calculation.

Some details of the computed corner secondary flow at station 4 are shown in Fig. 9. Transverse velocity vector plots are given for three different levels of magnification in the corner region. The vector magnitudes are normalized for each plot and thus indicate only flow direction and relative magnitude within each plot. It can be seen from Fig. 9 that there is a triple vortex structure in the computed corner flow. The vortices are counter-rotating and have decreasing strength as the corner is approached. Typical velocities in the three plots shown are of the order of 0.1, 0.01 and 0.0005 times the freestream velocity. Finally, a comparison of computed results obtained using both a $k-\epsilon$ and mixing length turbulence models is given in Fig. 10. The two solutions shown are identical in every respect except for the turbulence model used. The computed streamwise and transverse velocity fields are shown in Fig. 10 for station 4, which is downstream of the leading edge. Although some difference between the two solutions is evident in the streamwise velocity contours very near the corner, the transverse velocity away from the corner is not affected by this difference, and overall the two turbulence models give similar results.

CONCLUDING REMARKS

Solutions of the three-dimensional Reynolds-averaged Navier-Stokes equations have been computed for turbulent flow past a strut/endwall configuration for which experimental measurements are available. Computed results were obtained for both two-equation ($k-\epsilon$) and mixing length turbulence models. A key feature of the present calculations is that grid distributions which provide resolution of the viscous sublayer regions were used, as are believed important for three-dimensional flows of this type. There is good overall qualitative agreement between the computed and measured flow structures. The location of the initial saddle-point flow separation agrees well with the experimental flow visualization. The strength and scale of the mean flow velocities agrees with measurements, especially within the reversed flow region upstream of the leading edge. Computer-generated particle lines show a saddle-point separation followed by a strong downflow toward the endwall, and a reversed flow region, all of which are similar to numerous flow visualization experiments for horseshoe vortex flows. The computed corner flow has a multiple vortex structure. There are quantitative differences between

computed and measured velocities in the corner flow region, where the secondary vortex is relatively weak. These differences are likely due to the turbulence model used, and possibly numerical error. Computationally, it is significant that these solutions, with highly stretched meshes to provide viscous sublayer resolution, required only 100-200 iterations for convergence using a $60 \times 50 \times 40$ grid (120,000 points).

REFERENCES

1. Briley, W.R. and McDonald, H.: Computation of Three-Dimensional Horseshoe Vortex Flow Using the Navier-Stokes Equations. Seventh Int. Conf. on Num. Methods in Fluid Dyn., Stanford, 1980.
2. Briley, W.R. and McDonald, H.: Computation of Turbulent Horseshoe Vortex Flow Past Swept and Unswept Leading Edges. SRA Report R82-920001-F, 1982.
3. Briley, W.R., Buggeln, R.C. and McDonald, H.: Solution of the Three-Dimensional Navier-Stokes Equations for a Steady Laminar Horseshoe Vortex Flow. AIAA Paper No. 85-1520-CP, 1985.
4. McMahon, H., Hubbartt, J. and Kubendran, L.R.: Mean Velocities and Reynolds Stresses Upstream of a Simulated Wing-Fuselage Junction, NASA CR-3695, 1983.
5. Moore, J. and Forlini, T.J.: A Horseshoe Vortex in a Duct, J. Engr. for Gas Turbines and Power, Vol. 106, 1984, p. 668.
6. Eckerle, W.A. and Langston, L.S.: Measurements of a Turbulent Horseshoe Vortex Formed Around a Cylinder, NASA CR-3986, 1986.
7. Dickinson, S.C.: Flow Visualization and Velocity Measurements in the Separated Region of an Appendage-Flate-Plate Junction. David Taylor Naval Ship Research and Development Center Report DTNSRDC-86/020, 1986
8. Moore, J.G. and Moore, J.: Calculation of Horseshoe Vortex Flow Without Numerical Mixing. ASME Paper No. 84-GT-241, 1984.
9. Hung, L.M. and Kordulla, W.: A Time-Split Finite Volume Algorithm for Three-Dimensional Flow Field Simulation, AIAA Paper 83-1957, 1983.
10. Briley, W.R., McDonald, H. and Shamroth, S.J.: A Low Mach Number Euler Formulation and Application to Time-Iterative LBI Schemes, AIAA Journal, Vol. 21, No. 10, October 1983, p. 1467.
11. Kaplan, W.: Advanced Calculus, Addison-Wesley Publishing Company, Inc., 1952.
12. Jones, W.P. and Launder, B.E.: The Calculation of Low-Reynolds Number Phenomena With a Two-Equation Model of Turbulence. Int. J. Heat Mass Transfer, Vol. 16, pp. 1119-1130, 1973.
13. Launder, B.E. and Spalding, D.B.: The Numerical Computation of Turbulent Flows. Computer Methods in Appl. Mech. and Engr., Vol. 3, pp. 269-289, 1974.
14. McDonald, H. and Fish, R.W.: Practical Calculations of Transitional Boundary Layers. Int. J. Heat Mass Transfer, Vol. 16, pp. 1729-1744, 1973.

REFERENCES (Continued)

15. Briley, W.R. and McDonald, H.: Solution of the Multidimensional Compressible Navier-Stokes Equations by a Generalized Implicit Method, J. Comp. Physics, Vol. 24, August 1977, p. 372.
16. Briley, W.R. and McDonald, H.: On the Structure and Use of Linearized Block Implicit and Related Schemes, J. Comp. Physics, Vol. 34, 1980, p. 54.
17. Douglas, J. and Gunn, J.E.: A General Formulation of Alternating Direction Methods, Numerische Math., Vol. 6, 1964, p. 428.
18. Warming, R.F. and Beam, R.M.: On the Construction and Application of Implicit Factored Schemes for Conservation Laws, Symposium on Computational Fluid Dynamics, New York, April 1977; SIAM-AMS Proceedings, Vol. 11, 1977.
19. Beam, R.M. and Warming, R.F.: An Implicit Factored Scheme for the Compressible Navier-Stokes Equations. AIAA Journal, Vol. 16, 1978, p. 393.
20. Pulliam, T.H. and Steger, J.L.: Implicit Finite Difference Simulations of Three-Dimensional Compressible Flow, AIAA Journal, Vol. 18, 1980, p. 159.
21. Thomas, P.D. and Lombard, C.K.: Geometric Conservation Law and Its Application to Flow Computations on Moving Grids, AIAA Journal, Vol. 17, 1979, p. 1030.
22. Shamroth, S.J., McDonald, H. and Briley, W.R.: Prediction of Cascade Flow Fields Using the Averaged Navier-Stokes Equations, J. Engr. for Gas Turbines and Power, 1984, Vol. 106, p. 383.

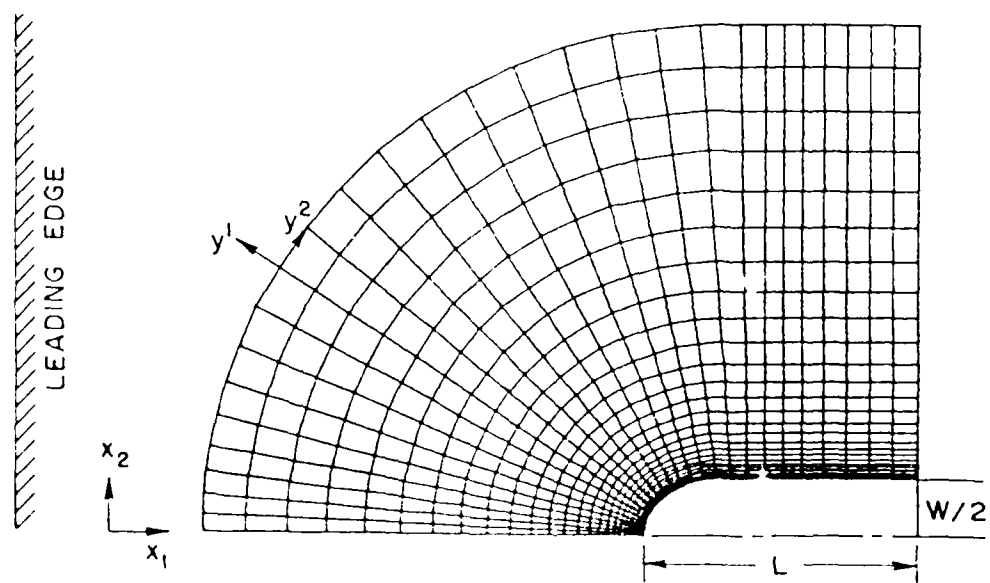
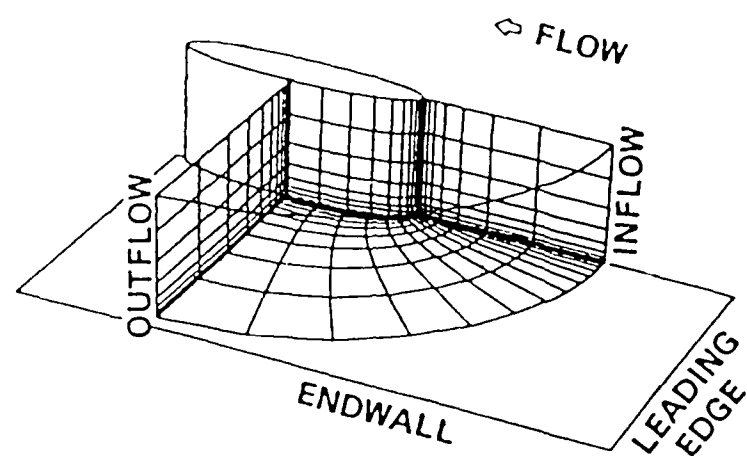


Fig. 1 - Flow Geometry and Coordinate System.

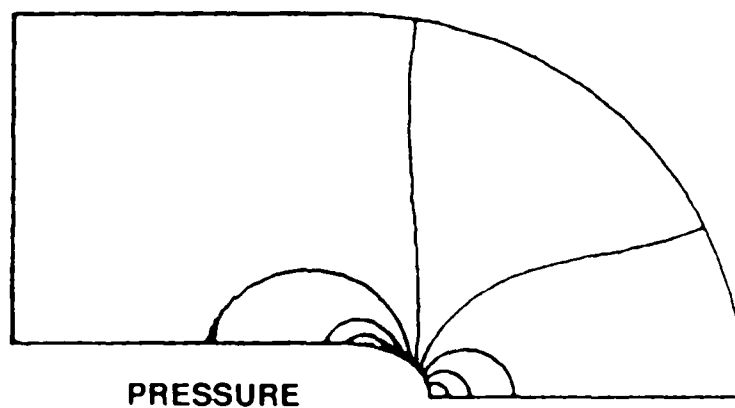
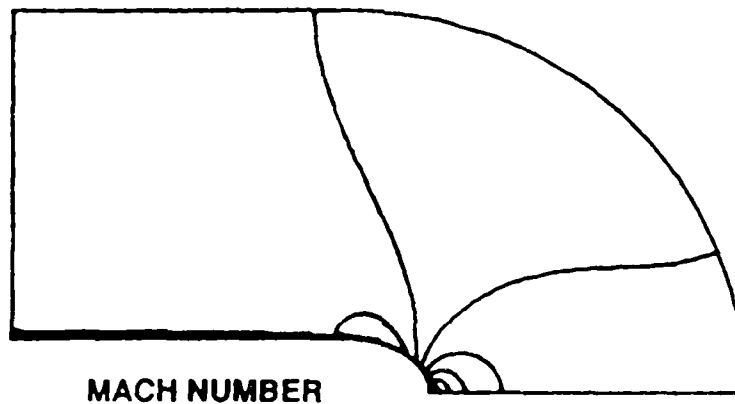
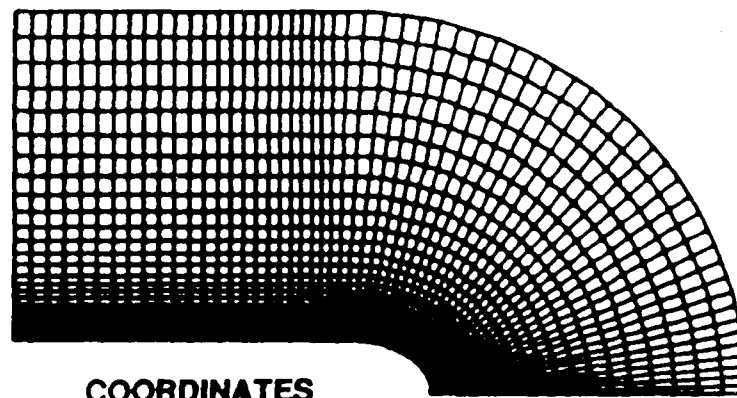


Fig. 2 - Test Calculations for 2D Turbulent Leading-Edge Flow.

LBI SCHEME - CONVERGENCE BEHAVIOR
2-D TURBULENT LEADING EDGE

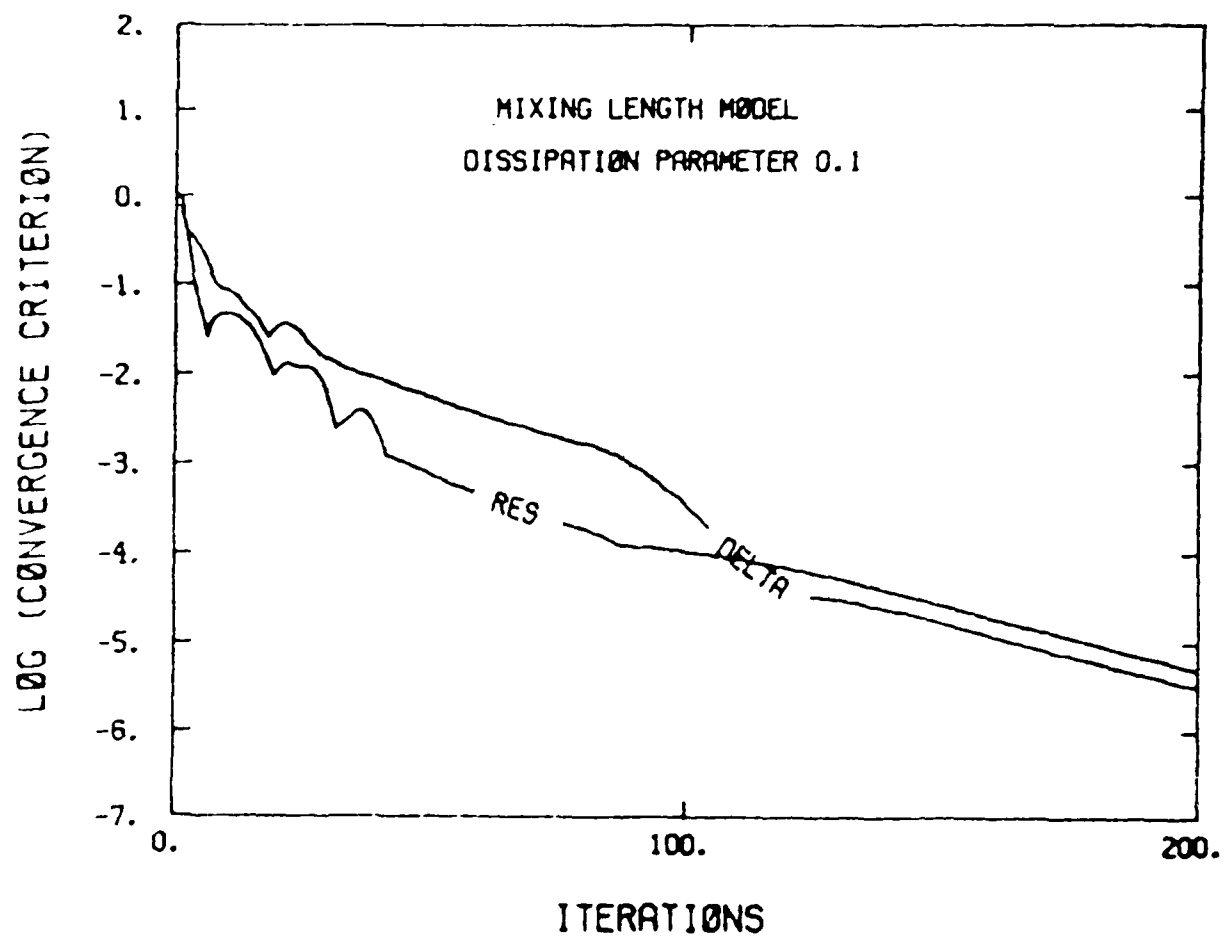


Fig. 3 - Convergence Behavior for Two-Dimensional Test Problem with Mixing Length Turbulence Model.

LBI SCHEME - CONVERGENCE BEHAVIOR
2-D TURBULENT LEADING EDGE

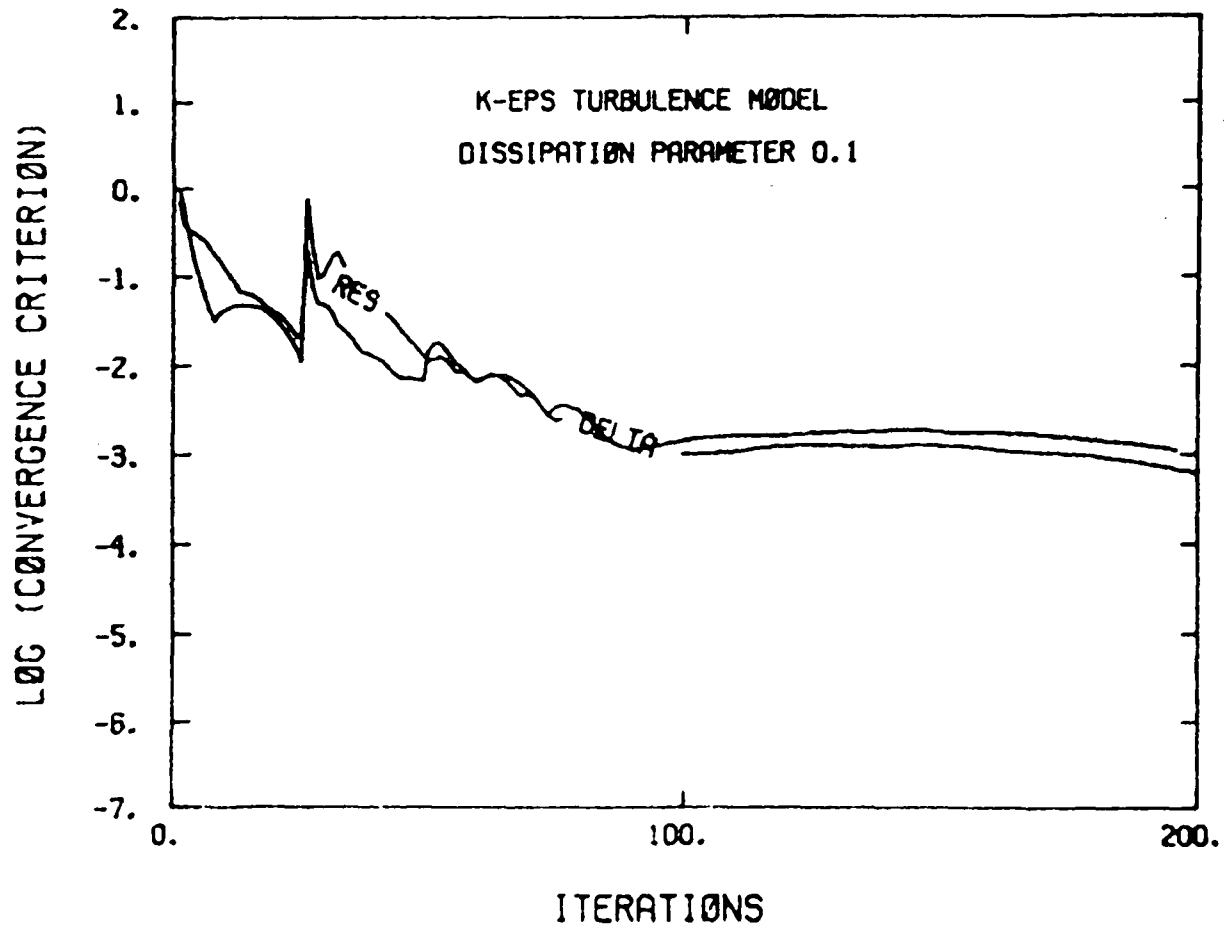


Fig. 4 - Convergence Behavior for Three-Dimensional
Test Problem with k- ϵ Turbulence Model.

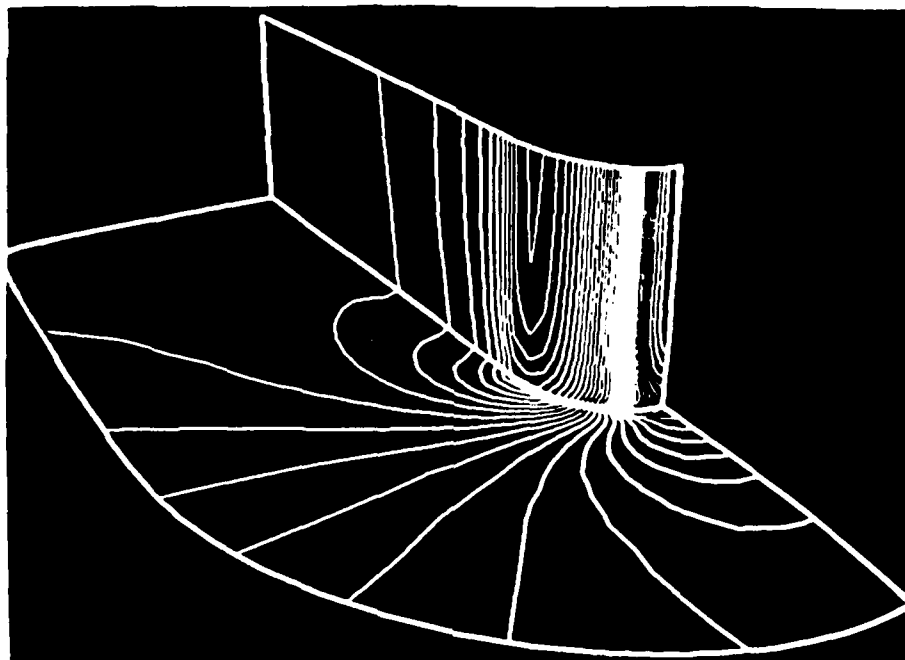
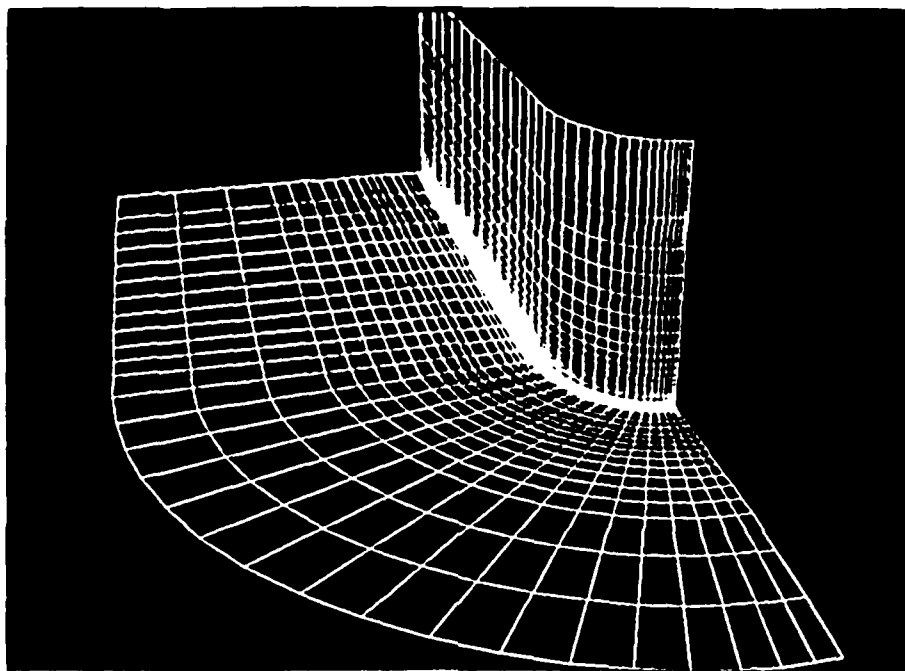


Fig. 5a - Computational Grid and Surface Pressure contours.

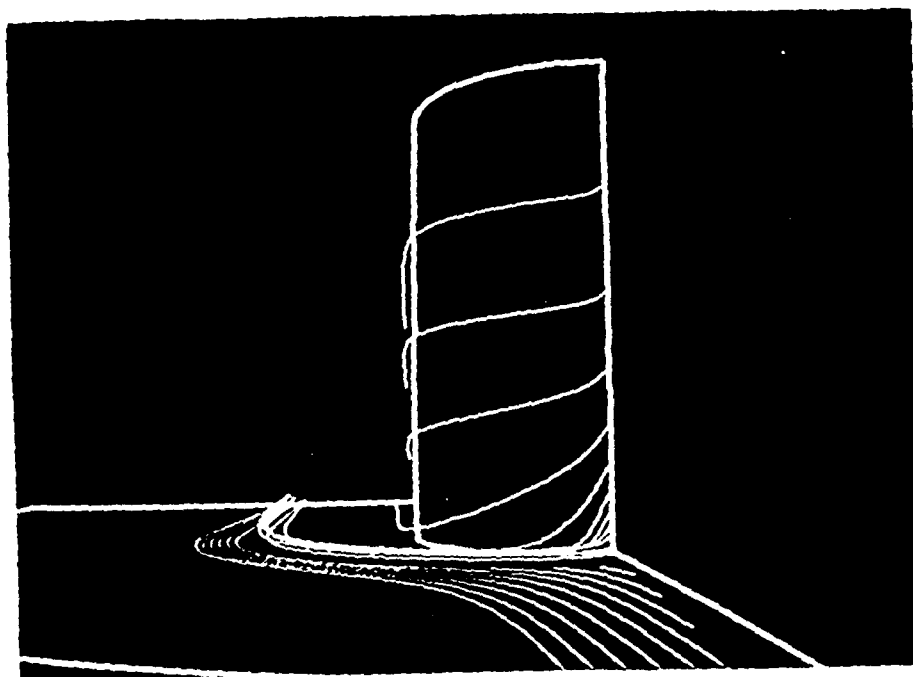
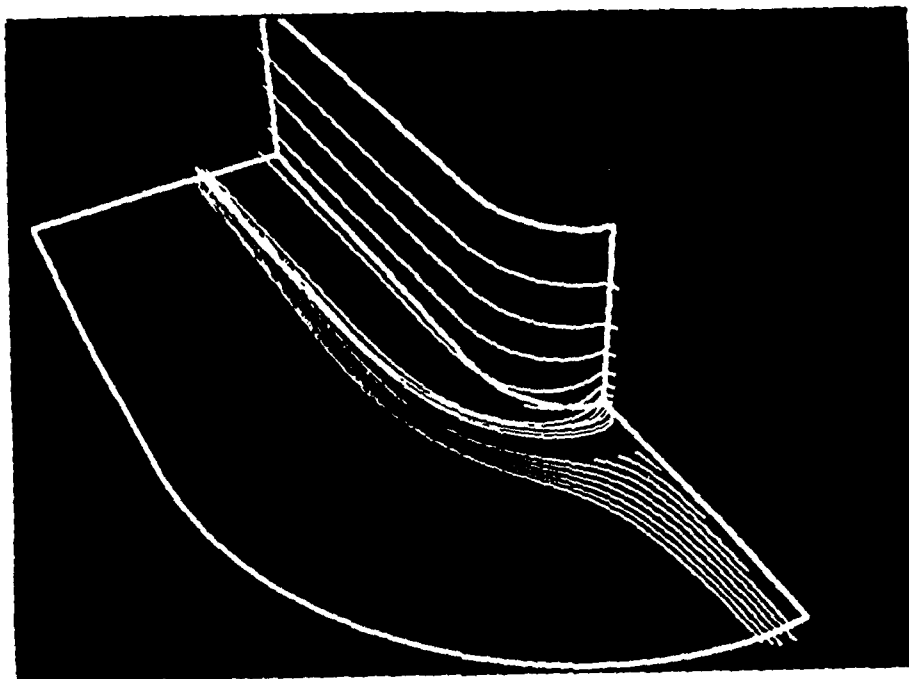


Fig. 58 - Particle Path Lines.

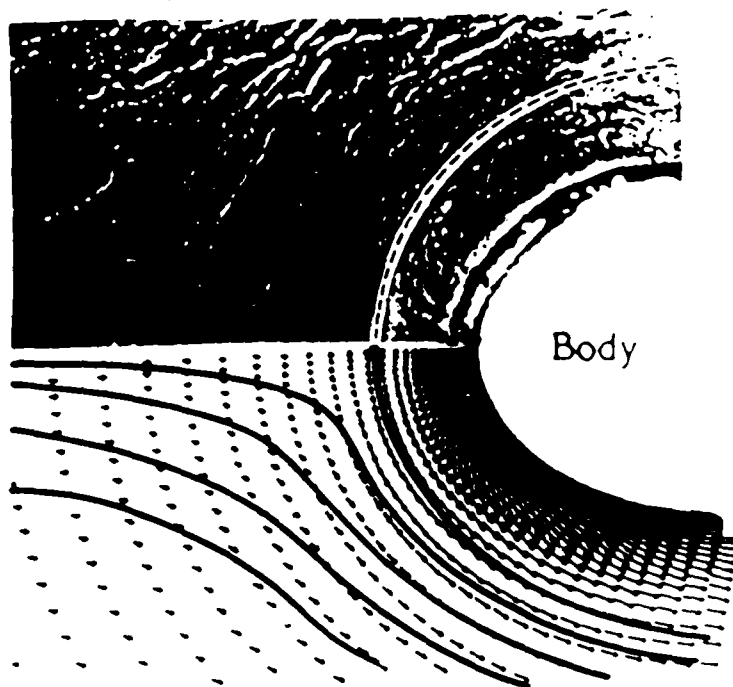
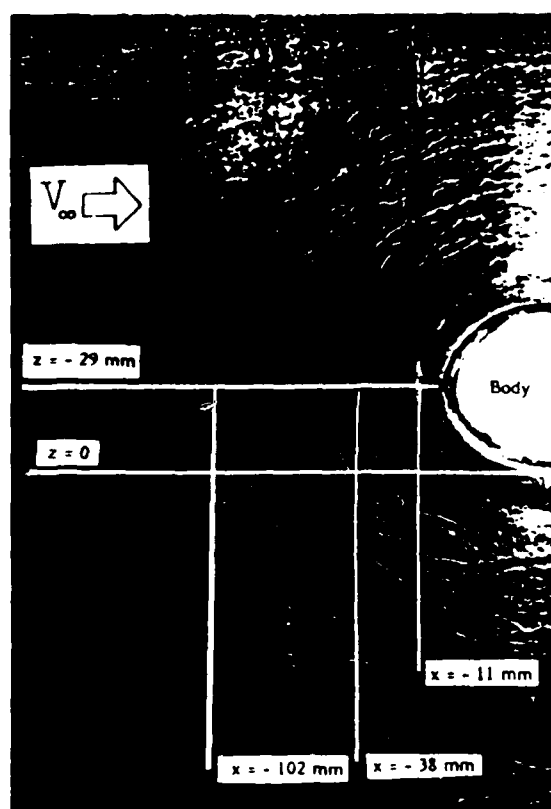


Fig. 6 - Surface Flow Visualization (Comparison with Experimental Results of Ref. 4).

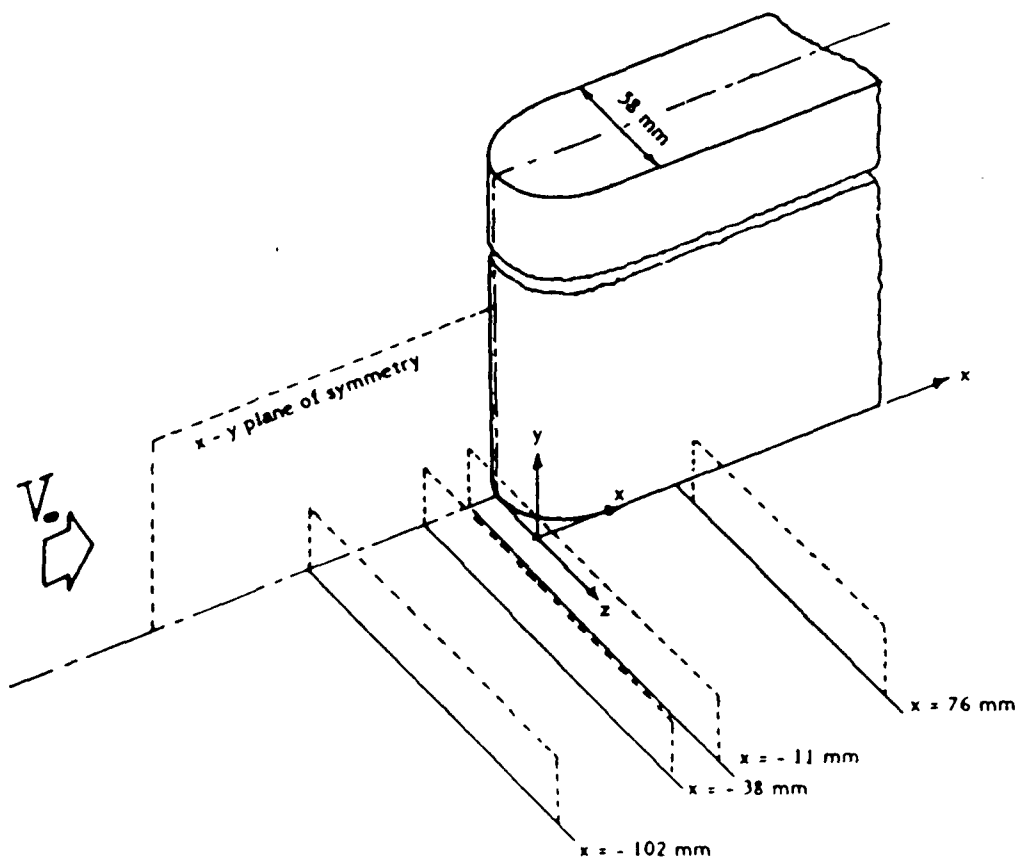
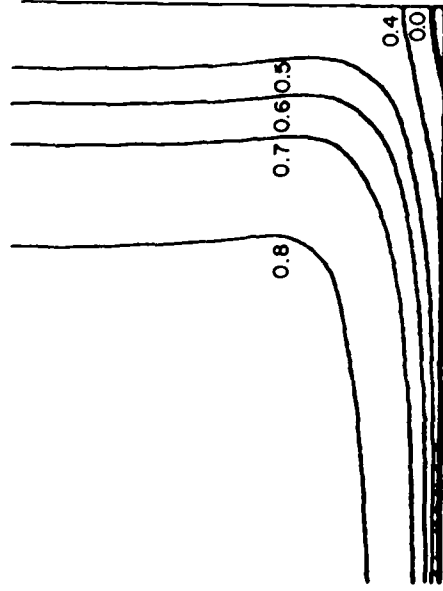


Fig. 7 - Geometry and Measuring Stations (From Ref. 4).

COMPUTED



MEASUREMENTS

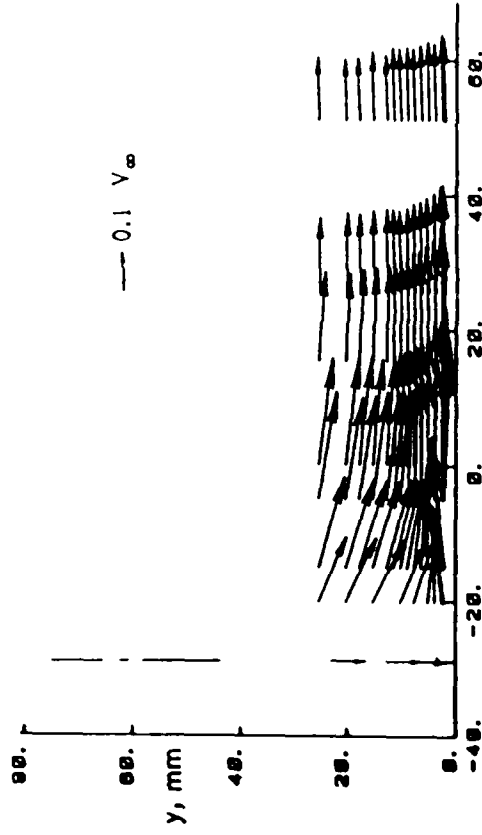
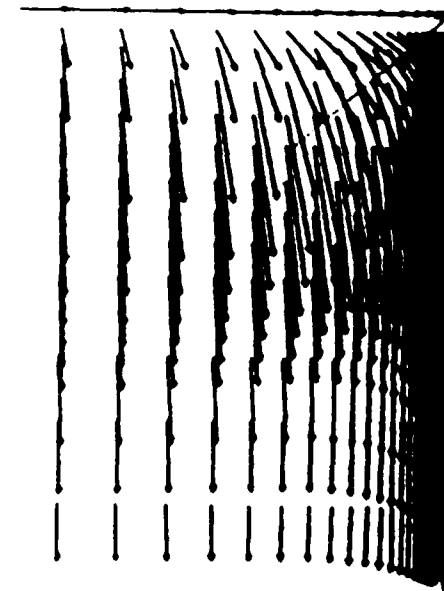
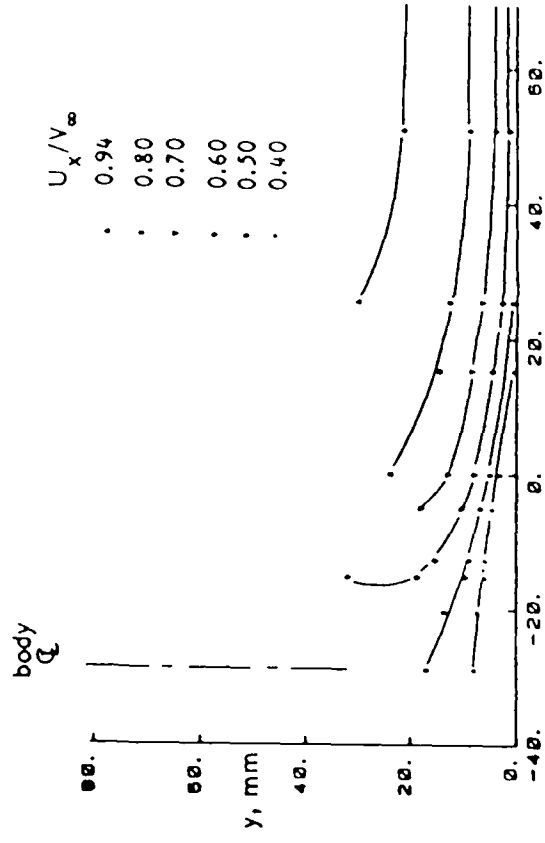


Fig. 8a - Comparison of Computed and Measured Velocity at Station 3 (-11 mm).

COMPUTED



MEASUREMENTS

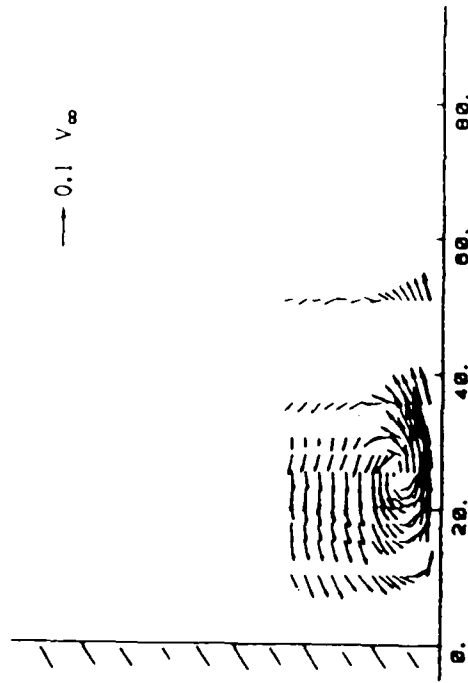
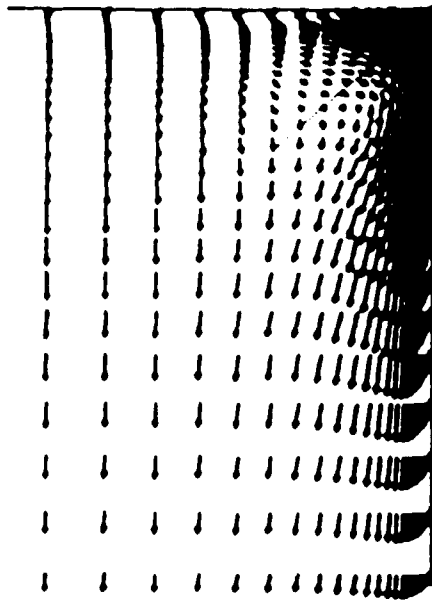
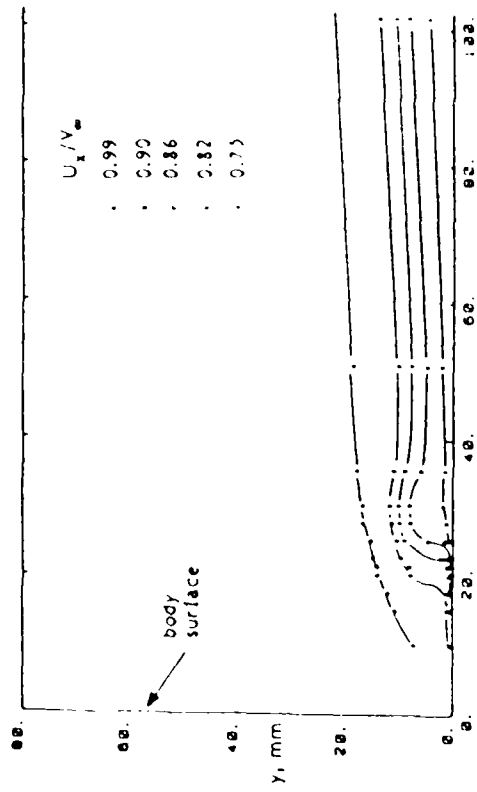
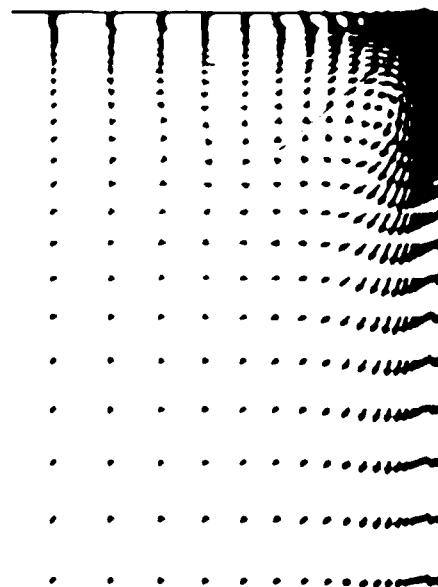


Fig. 8b - Comparison of Computed and Measured Velocity at Station 4 (76 mm).

COMPUTED



MEASUREMENTS

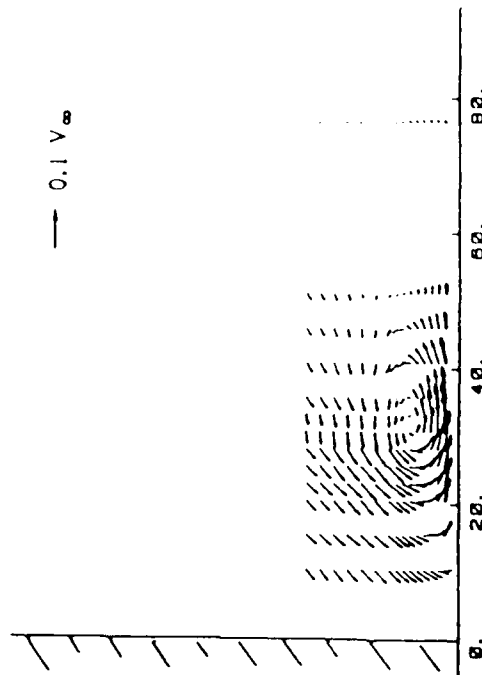
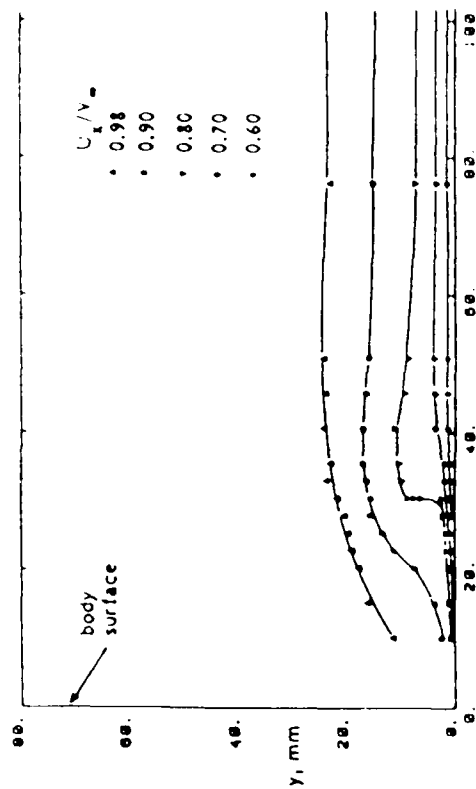


Fig. 8c - Comparison of Computed and Measured Velocity at Station 5 (165 mm).

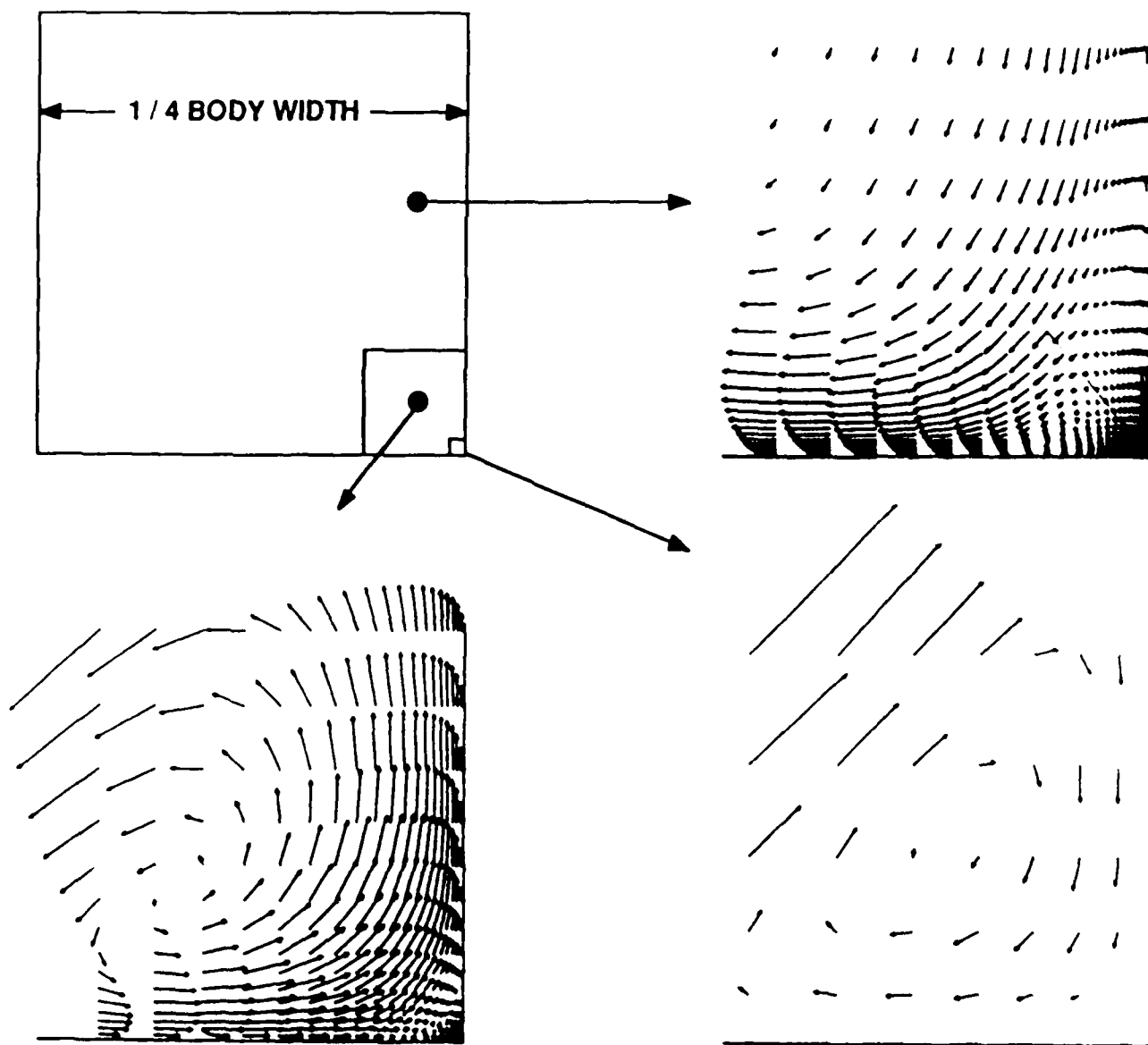
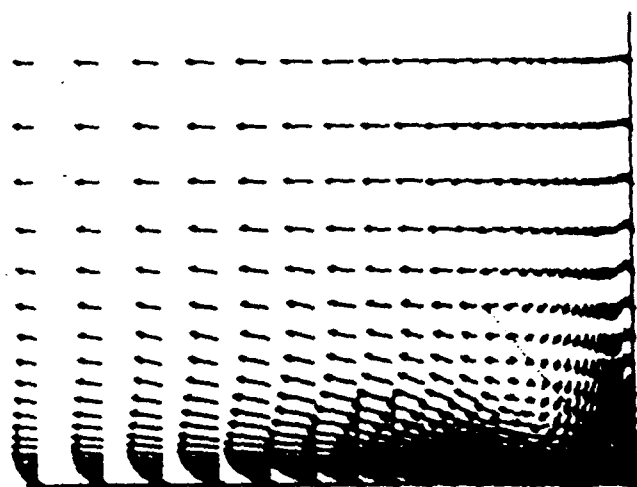
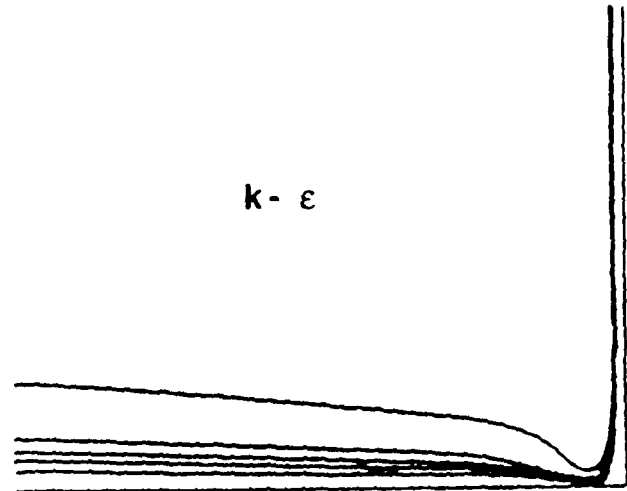


Fig. 9 - Details of Corner Secondary Flow at Station 4 (76 mm).



k- ϵ



MIXING
LENGTH

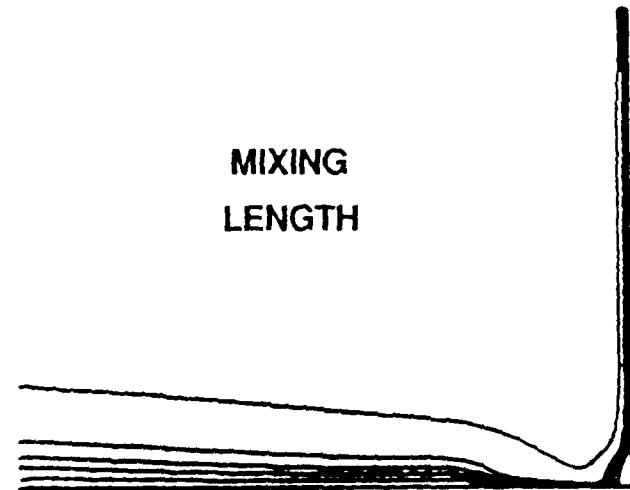


Fig. 10 - Comparison of Mixing Length and k- ϵ Results at Station 4 (76 mm).

END

3-87

Dtic